Climatological Characteristics of Raindrop Size Distributions in Busan, Korea

Sung-Ho SUH[1]

Cheol-Hwan YOU[2*]

Email: youch@pknu.ac.kr

Dong-In LEE[1,2]

Institutional addresses:

[1] Department of Environmental Atmospheric Sciences, Pukyong National University, Daeyeon campus 45, Yongso-ro, Namgu, Busan 608-737 Republic of Korea

[2]Atmospheric Environmental Research Institute, Daeyeon campus 45, Yongso-ro, Namgu, Busan 608-737 Republic of Korea

* Corresponding author

Abstract

Raindrop size distribution (DSD) characteristics within the complex area of Busan, Korea (35.12°N, 129.10°E) were studied using a Precipitation Occurrence Sensor System (POSS) disdrometer over a four-year period from February 24th 2001 to December 24th 2004. Also, to find the dominant characteristics of polarized radar parameters which is differential radar reflectivity (Z_{dr}), specific differential phase (K_{dp}) and specific attenuation (A_h), T-matrix scattering simulation was applied in present study. To analyze the climatological DSD characteristics in more detail, the entire period of recorded rainfall was divided into 10 categories not only cover different temporal and spatial scales, but different rainfall types. When only convective rainfall was considered, mean value of mass weighted mean diameter (D_m) and normalized number concentration (N_w) values for all these categories converged around a maritime cluster, except for rainfall associated with Typhoons. The convective rainfall of a Typhoon showed much smaller D_m and larger N_w compared with the other rainfall categories.

In terms of diurnal DSD variability, we observe maritime (continental) precipitation during the daytime (DT) (nighttime, NT), which likely results from sea (land) wind identified through wind direction analysis. These features also appeared in the seasonal diurnal distribution. The DT and NT Probability Density Function (PDF) during the Summer was similar to the PDF of the entire study period. However, the DT and NT PDF during the Winter season displayed an inverse distribution due to seasonal differences in wind direction.

Keyword: DSD, POSS disdrometer, Climatological characteristics, Land and sea wind

1. Introduction

Drop Size Distribution (DSD) is controlled by the microphysical processes of rainfall and therefore plays an important role in the development of quantitative rainfall estimation algorithms based on forward scattering simulations of radar measurements (Seliga and Bringi, 1976). DSD data accurately reflect local rainfall characteristics within an observation area (You et al., 2014). Many DSD models have been developed to characterize spatial-temporal differences in DSDs under various atmospheric conditions (Ulbrich, 1983). Marshall and Palmer (1948) developed an exponential DSD model using DSD data collected by a filter paper technique ($\mathrm{N(D)} = 8 \times 10^{3}\,\exp(-410\mathrm{R}^{-0.21}\mathrm{D})$ in $\mathrm{m^{-3}mm^{-1}}$, D in mm and R in mm $\mathrm{h^{-1}}$). In subsequent studies, a lognormal distribution was assumed to overcome the problem of exponential DSD mismatching with real data (Mueller, 1966; Levin, 1971; Markowitz, 1976; Feingold and Levin, 1986).

To further investigate natural DSD variations, Ulbrich (1983) developed a gamma DSD that permitted changing the dimension of the intercept parameter ($\mathrm{N_0}$ in $\mathrm{m^{-3}\,mm^{-1-\mu}}$) with ($\mathrm{N(D)} = \mathrm{N_0 D^{\mu}}\exp(-\Lambda \mathrm{D})$). In addition, to enable the quantitative analysis of different rainfall events, the development of a normalized gamma DSD model that accounted for the independent distribution of DSD from the disdrometer channel interval enabled a better representation of the actual DSD (Willis, 1984; Dou et al., 1999; Testud et al., 2001).

DSDs depend on the rainfall type, geographical and atmospheric conditions, and observation time, and are closely linked to microphysical characteristics that control rainfall development mechanisms. In the case of stratiform rainfall, raindrops grow by accretion because of the relatively long residence time in weak updrafts, in which almost all water droplets are changed to ice particles. With time, the ice particles grow sufficiently and fall to the ground. The raindrop size of stratiform rainfall observed at the ground level is larger than that of convective rainfall for a same rainfall rate due to the resistance of the ice particles to break-up mechanisms. In contrast to stratiform rainfall, in convective rainfall raindrops grow by the collision-coalescence mechanism associated with relatively strong vertical wind speeds and short residence time in the cloud. Fully-grown raindrops of maritime precipitation are smaller in diameter than those in stratiform rainfall due to the break-up mechanism in case of same rainfall rate (Mapes and Houze Jr, 1993; Tokay and Short, 1996). Convective rainfall can be classified into two types based on the origin and direction of movement. Rainfall systems occurring over ocean and land are referred to as maritime and continental rainfall, respectively (Göke et al., 2007). Continental rainfall is related to a cold-rain mechanism whereby raindrops grow in the form of ice particles. In contrast, maritime rainfall is related to a warm-rain mechanism whereby raindrops grow by the collision-coalescence mechanism. Therefore, the mass-weighted drop diameter (D_m) of continental rainfall observed on the ground is larger than that of maritime rainfall, and a smaller normalized intercept parameter (N_w) is observed in continental rainfall (Bringi et al., 2003).

Specific heat is a major climatological feature that creates differences between DSDs in maritime and continental regions. These two regions have different thermal capacities and thus display different temperature variations with time. The surface temperature of the ocean changes slowly because of the water’s high thermal capacity, while the continental regions, which have comparatively lower thermal capacity, display greater diurnal variability. Sea winds generally is occurred in from afternoon to early evening when the temperature gradient between the sea and land becomes negative, which is the opposite of the gradient in the daytime (DT). In coastal regions, the land and sea wind effect causes a pronounced difference between the DT and nighttime (NT) DSD characteristics. Also, when mountains are located near the coast, the difference is intensified by mountain and valley winds (Qian, 2008).

In the present study, we analyzed a four-year dataset spanning from 2001 to 2004, collected from Busan, Korea (35.12°N, 129.10°E) using a Precipitation Occurrence Sensor System (POSS) disdrometer, to investigate the characteristics of DSDs in Busan, Korea which consist complex mid-latitude region comprising both land and ocean. To quantify the effect of land and sea wind on these characteristics, we also analyzed diurnal variations in DSDs. The remainder of the manuscript is organized as follows. In Section 2 we review the normalized gamma model and explain the DSD quality control method and the classification of rainfall. In Section 3 we report the results of DSD analysis with respect to stratiform/convective and continental/maritime rainfall, and discuss diurnal variations. Finally, a summary of the results and the main conclusions are presented in Section 4.

2. Data and Methods

2.1. Normalized Gamma DSD

The DSD is defined by $\mathrm{N(D)} = \mathrm{N_0} \exp(-\Lambda \mathrm{D})$ $(\mathrm{m^{-3} mm^{-1}})$ and the one of the methods to reflect the microphysical characteristics of rainfall using the number concentration of rainfall drops. Also, DSD is able to calculate the many kind of parameters which show the dominant feature of raindrops. Normalization is used to define the DSD and to solve the non-independence of each DSD parameter (Willis, 1984; Dou et al., 1999; Testud et al., 2001). Furthermore, a normalized gamma DSD enables the comparison of quantitative estimations for cases of rainfall events that have different time scales and rain rates. Here, we use the DSD model designed by Testud et al. (2001):

$$N(D) = N_w f(\mu)(\frac{D}{D_m})^{\mu} \exp\left[-(4+\mu)\frac{D}{D_m}\right]. \qquad (1)$$

where D is volume equivalent spherical raindrop size (mm), and $f(\mu)$ is defined using the DSD model shape parameter (μ) and gamma function (Γ) as follows:

$$f(\mu) = \frac{6}{4^4}\frac{(\mu+4)^{4+\mu}}{\Gamma(4+\mu)}. \qquad (2)$$

From the value of $N(D)$, the median volume diameter (D_0 in mm) can be obtained as follows:

$$\int_0^{D_0} D^3 N(D)dD = \frac{1}{2}\int_0^{D_{max}} D^3 N(D)dD. \qquad (3)$$

Mass-weighted mean diameter (D_m in mm) is calculated as the ratio of the fourth to the third moment of the DSD:

$$D_m = \frac{\int_0^{D_{max}} D^4 N(D)dD}{\int_0^{D_{max}} D^3 N(D)dD}. \qquad (4)$$

The normalized intercept parameter (N_w in $m^{-3}mm^{-1}$) is calculated as follows:

$$N_w = \frac{4^4}{\pi\rho_w}\left(\frac{LWC}{D_m^4}\right). \quad (5)$$

The shape of the DSD is calculated as the ratio of D_m to the standard deviation (SD) of D_m (σ_m in mm) (Ulbrich and Atlas, 1998; Bringi et al., 2003; Leinonen et al., 2012):

$$\sigma_m = \left[\frac{\int_0^{D_{max}} D^3(D-D_m)^2 N(D)dD}{\int_0^{D_{max}} D^3 N(D)dD}\right]^{\frac{1}{2}}. \quad (6)$$

In addition, σ_m/D_m is related to μ as follows:

$$\frac{\sigma_m}{D_m} = \frac{1}{(4+\mu)^{1/2}}. \quad (7)$$

Liquid water content (LWC in $g\ m^{-3}$) can be defined from the estimated DSD:

$$LWC = \frac{\pi}{6}\rho_w \int_0^{D_{max}} D^3 N(D)dD. \quad (8)$$

where ρ_w is water density ($\mathrm{g\ m^{-3}}$) and it assumed as $1\ \mathrm{g\ m^{-3}}$ for a liquid water. Similarly, rainfall rate (R in $\mathrm{mm\ h^{-1}}$) can be defined as follows:

$$\mathrm{R} = \frac{3.6}{10^3}\frac{\pi}{6}\int_0^{\mathrm{D_{max}}} \mathrm{v(D)D^3N(D)dD}. \quad (9)$$

where the value of factor 3.6×10^3 is the unit conversion which converts the mass flux unis ($\mathrm{mg\ m^{-2}\ s^{-1}}$) to the common unit ($\mathrm{mm\ h^{-1}}$) for the convenience. $\mathrm{v(D)}$ ($\mathrm{m\ s^{-1}}$) is the fall velocity for each raindrop size. The relationship between $\mathrm{v(D)}$ and equivalent spherical raindrop size (D in mm) is given by Atlas et al. (1973) who developed an empirical formula based on the data reported by Gunn and Kinzer (1949):

$$\mathrm{v(D)} = 9.65 - 10.3\exp[-0.6\mathrm{D}]. \quad (10)$$

2.2 Quality Control of POSS Data

POSS was used to measure the number of raindrops within the diameter range of 0.34-5.34 mm, using bistatic, continuous wave X-band Doppler radar (10.525 GHz) across 34 channels (Fig. 1; Sheppard and Joe, 2008). Using estimated DSD, Doppler power density spectrum is generated as follows;

$$S(f) = \int_{D_{min}}^{D_{max}} N(D_m)V(D_m, \rho, h, w)\bar{S}(f, D_m, \rho, h, w)dD_m. \quad (11)$$

Where $S(f)$ means Doppler spectrum power density, $V(D_m, \rho, h, w)\bar{S}(f, D_m, \rho, h, w)$ means weighting function of $S(f)$, $\bar{S}$ is the mean of $S(f)$, ρ is density of precipitation distribution, h is the shape of precipitation distribution, w ($m\ s^{-1}$) is wind speed and $V(x)$ is sample volume. A Doppler power density spectrum has a resolution of 16Hz and terminal velocity (v_t) has a resolution of 0.24 $m\ s^{-1}$. Transmitter and receiver skewed about 20° toward each other, and cross point of signal is located over 34 cm from transmitter-receiver. Transmitter-receiver toward upper side detects $N(D)$ of raindrops in observation volume ($V(D)$) (Sheppard, 1990). Also, Sheppard (1990) and Sheppard and Joe (1994) noted some shortcomings as the overestimation of small drops at horizontal wind larger than 6 $m\ s^{-1}$. However, in present study, the quality control of POSS for wind effect does not consider because of beyond the research. Detailed specifications and measurement range and raindrop size for each observation channel of the POSS disdrometer are summarized in Table 1.

A POSS disdrometer was installed in Busan, Korea (35.12°N, 129.10°E), along with other atmospheric instruments, the locations of which are shown in Fig. 2. Estimating raindrop size correctly is challenging and care should be taken to ensure reliable data are collected. We performed the following quality controls to optimize the accuracy of the disdrometer estimates. i) Non-liquid type event data (e.g., snow, hail etc.) detected by POSS were excluded, to focus only on liquid state rainfall. ii) Non-atmospheric data were removed from the analysis if the number of DSD spectra was smaller than five consecutive channels, or the position of DSD spectra only detected in smaller (larger) than the 5^{th} (10^{th}) channel for each 1-min channel data.

iii) Only data recorded in more than 10 complete channels were considered. iv) To compensate for the reduced capability to detect raindrops smaller than 1 mm when R > 200 mm h^{-1} (as recorded by the disdrometer), data collected when R > 200 mm h^{-1} were not included in the analyses. v) To eliminate wind and acoustic noise, data collected when R < 0.1 mm h^{-1} were removed (Tokay and Short, 1996). vi) The value of D_0 which is calculated by Eq. (3) tends to be overestimated when D_0 < 0.5 mm (Leinonen et al., 2012). Because the correlation coefficient between D_0 and D_m was 0.985 for the whole study period, we considered that D_m could be used for the analysis instead of D_0.

After performing all quality control procedures, 99,388 spectra were left from an original total of 166,682 for 1-min temporal resolution. Accumulated rainfall amount from POSS during the entire period was 4261.49 mm. To verify the reliability of the POSS data, they were compared with data collected by a 0.5 mm tipping bucket rain gaugeat an automatic weather system (AWS) located ~368 m from the POSS (Fig. 3).

2.3 Radar Parameters

To derive the rainfall relations, polarized parameters were computed by a T-matrix scattering simulation (Waterman, 1971; Zhang et al., 2001). First, the radar reflectivity factor (z, mm^6m^{-3}) and non-polarized radar reflectivity (Z, dBZ) were computed using the DSD data collected by POSS, as follows:

$$z = \int_0^{D_{max}} D^6 N(D) dD. \tag{12}$$

$$Z = 10\log_{10}(z). \quad (13)$$

Axis ratios of raindrops differ with atmospheric conditions and rainfall type. To derive the drop shape relation from the drop diameter, we applied the results of numerical simulations and wind tunnel tests employing a forth-polynomial equation, as in many previous studies (Beard and Chuang, 1987; Pruppacher and Beard, 1970; Andsager et al., 1999; Brandes et al., 2002). The drop-shape relation used in the present study is a combination of those from Andsager et al. (1999) and Beard and Chuang (1987) for three raindrop size ranges (Bringi et al., 2003). The raindrop axis ratio relation of Andsager et al. (1999) is applied in the range of $1 < \mathrm{D\ (mm)} < 4$, as follows:

$$r = 1.0048 + 0.0057D - 2.628D^2 + 3.682D^3 - 1.677D^4. \quad (14)$$

The drop-shape relation of Beard and Chuang (1987) is applied in the range of $D < 1$ mm and $D > 4$ mm, as follows:

$$r = 1.012 + 0.01445D - 0.01028D^2. \quad (15)$$

We assumed SD and the mean canting angle of raindrops as $7°$ and $0°$, respectively. The refractive indices of liquid water at 20 ℃ were used (Ray, 1972). Also, the condition of frequency for electromagnetic wave of radar is 2.85 GHz (S-band). We calculated dual polarized radar parameters based on these conditions. The parameters of differential reflectivity, $\mathrm{Z_{dr}}$ (dB), specific differential phase, $\mathrm{K_{dp}}$ ($\mathrm{deg\,km^{-1}}$), and attenuation, $\mathrm{A_h}$ ($\mathrm{dB\,km^{-1}}$), using DSD data were calculated and analyzed.

2.4. Classification of Rainfall Types and Rainfall Events

Rainfall systems can be classified as stratiform or convective in nature, via analysis of the following microphysical characteristics: i) DSD, using relationships between $\mathrm{N_0}$ and R ($\mathrm{N_0} = 4 \times 10^9 \mathrm{R}^{4.3}$ in $\mathrm{m^{-3} mm^{-1}}$(Tokay and Short, 1996; Testud et al., 2001); ii) radar reflectivity, where, according to Gamache and Houze (1982), a rainfall system that displays radar reflectivity larger than 38 dBZ is considered to be convective; and iii) rainfall rate, where average 5-min R > 0.5 $\mathrm{mm\,h^{-1}}$ is considered convective rainfall (Johnson and Hamilton, 1988). Alternatively, rainfall that has 1-min R > 5 (0.5) $\mathrm{mm\,h^{-1}}$ and a SD of R > (<) 1.5 $\mathrm{mm\,h^{-1}}$ is considered as convective (stratiform) type (Bringi et al., 2003). The rainfall classification method proposed by Bringi et al. (2003) is applied in the present study.

It is necessary to categorize different rainfall systems because their microphysical characteristics show great variation depending on the type of rainfall, as well as the type of rainfall event; e.g., Typhoon, Chanma, heavy rainfall and seasonally discrete rainfall. To investigate the temporal variation in DSDs, we analyzed daily and seasonal DSDs. Likewise, to investigate diurnal variability in DSD, DT and NT data were considered by using the sunrise and sunset time in Busan (provided by the Korea Astronomy and Space Science Institute [KASI]). In the middle latitudes, and including Busan, the timings of sunrise and sunset vary due to solar culminating height. The earliest and latest sunrise (sunset) time of the entire period is 0509 KST (1712 KST) and 0733 KST (1942 KST), respectively. DT (NT) is defined as the period from the latest sunrise (sunset) time to the earliest sunset (sunrise) time for the unity of classification of each time group (Table 2).

To analyze the predominant characteristics of DSDs for Typhoon rainfall, nine Typhoon events were selected from throughout the entire study period which is summarized in Table 2.

This study utilizes the Korea Meteorological Administration (KMA) rainfall warning regulations to identify heavy rainfall events. The KMA issues a warning if the accumulated rain amount is expected to be >70 mm within a 6-hour period, or >110 mm within a 12-hour period. Rainfall events classified as Chanma and Typhoon were not included in the classification 'heavy rainfall'.

Chanma is the localized rainfall system or rainy season that is usually present over the Korean Peninsula between mid-June and mid-July which is similar to the Meiyu (China) or Baiu (Japan). The selected dates and periods of each rainfall category are summarized in Table 2.

3. Results

3.1. DSD and Radar Parameters

Figure 4 shows the Probability Density Function (PDF) and Cumulative Distribution Function (CDF) of DSDs and radar parameters with respect to stratiform and convective rainfall. The PDFs of DSD and radar parameters were calculated using the non-parameterization kernel estimation to identify the dominant distribution of each parameter recorded in Busan. Non-parameterization kernel estimation was also used to identify continuous distributions of DSDs. The PDF of stratiform rainfall is more similar to that of the dataset for the entire analysis period due to the dominant contribution of stratiform rainfall (about 62.93%) to the overall rainfall than that of convective rainfall. However, the PDF for convective rainfall is significantly different from that of the entire analysis period, and as the convective rainfall contributes only 6.11% of the overall rainfall (Table 3). When $\mu < 0$ the distribution of μ for convective rain has more value of PDF than that for stratiform rain (Fig. 4a). Alternatively, the frequency of μ for stratiform rainfall is higher than that of convective rainfall when $0 < \mu > 5$. The value of μ for convective rainfall is higher than that for stratiform rainfall because the break-up mechanism would be increase the number concentration of small raindrops. The number concentrations of mid-size raindrops increased due to the decrease in the number concentration of relatively large raindrops (Hu and Srivastava, 1995; Sauvageot and Lacaux, 1995). However, we observed a higher frequency of convective rainfall than stratiform rainfall in the negative μ range.

The PDF of D_m displays peak around 1.2 and 1.4 mm for stratiform rainfall and the entire rainfall dataset, respectively. We note that a gentle peak exists around 0.7 mm for both stratiform and convective rainfall datasets (Fig. 4b). These features are similar to the distribution of D_m observed in a high-latitude region at Järvenpää, Finland (Fig. 4 of Leinonen et al., 2012). For D_m values > 1.7 mm, the PDF for convective rainfall is higher than stratiform rainfall. Accordingly, the value of DSD for stratiform rainfall is higher than that of convective rainfall when $D_m < 1.7$ mm. Generally, stratiform rainfall that develops by the cold rain process displays weaker upward winds and less efficient break-up of raindrops. Therefore, in the same rainfall rate, stratiform rainfall tends to produce larger raindrops than convective rainfall that develops by the warm rain process. However, the average D_m values for convective and stratiform rain for the entire period are approximately 1.45 and 1.7 mm, respectively. In short, D_m is proportional to R regardless of rainfall type. This finding is consistent with the results of Atlas et al. (1999) who found that the D_m of convective rainfall is larger than that of stratiform rainfall on Kapingamarangi Island, Micronesia.

The PDF of $\log_{10}(N_w)$ for the entire rainfall dataset was evenly distributed between 1.5 and 5.5, with a peak at N_w = 3.3 (Fig. 4c). The PDF of $\log_{10}(N_w)$ for stratiform rainfall is rarely > 5.5, while for convective rainfall it is higher at > 5.5 than that of stratiform. There is a similar frequency in the stratiform and convective rainfall at 4.4

The PDF distributions for $\log_{10}(R)$ and $\log_{10}(LWC)$ are similar each other (Fig. 4d and e). It is infer that the similar results come from the using of alike moment of DSD as 3.67 and 3 for R and LWC, respectively. The PDF of $\log_{10}(R)$ for the entire rainfall dataset ranged between -0.5 and 2. A peak exists at 0.3 and the PDF rapidly decreases from the peak value as R increases. The PDF for stratiform rainfall has a higher frequency than that of the entire rainfall when -0.3 < $\log_{10}(R)$ < 0.7, while the PDF for convective rainfall is denser between 0.4 and 2. Furthermore, the frequency of the PDF for convective rainfall was higher than that of stratiform rainfall in case of $\log_{10}(R)$ > 0.65 and the peak value shown was 0.9.

The PDF and CDF for non-polarized reflectivity (Z), differential reflectivity (Z_{dr}), specific differential phase (K_{dp}), and specific attenuation of horizontal reflectivity (A_h) are shown in Fig. 4f-i. The PDF of Z_h for stratiform rainfall (Fig. 4f) is widely distribute between 10 and 50 dBZ with the peak at approximately 27 dBZ. Conversely, for convective rainfall, the value of PDF lie between 27 and 55 dBZ and the peak frequency value at approximately 41 dBZ. The frequency value of reflectivity is higher for convective rainfall than for stratiform rainfall in the range of ~ >35 dBZ. Furthermore, the shape of the PDF for convective rainfall is similar to that reported for Darwin, Australia (Steiner et al., 1995); however, for stratiform rainfall there are significant differences between Busan and Darwin in terms of the shape of the frequency distribution. The PDF of Z_{dr} for the entire rainfall primarily exists between 0 and 2.5 dB, and the peaks are at 0.3 and 1.8 dB (Fig. 4g). The distribution of Z_{dr} for convective and stratiform rainfall is concentrated between 0.6 and 1.6 dB, and between 0.3 and 2 dB, respectively. The frequency of Z_{dr} for convective (stratiform) rainfall exists in ranges higher (lower) than stratiform (convective) at 0.9 dB.

The dominant distribution of K_{dp} for the entire dataset and for stratiform rainfall lies between 0 and 0.14 $\mathrm{deg\,km^{-1}}$, with a peak value of 0.03 $\mathrm{deg\,km^{-1}}$ and 0.08 $\mathrm{deg\,km^{-1}}$. However, for convective rainfall the PDF of K_{dp} is evenly exist between 0.01 and 0.15 $\mathrm{deg\,km^{-1}}$. Furthermore, when K_{dp} > 0.056 $\mathrm{deg\,km^{-1}}$, the frequency of the PDF for convective rainfall is higher than that of stratiform rainfall (Fig. 4h).

The PDF of A_h is similar to that of K_{dp} and is exist between 0 and 0.01 $\mathrm{dB\,km^{-1}}$. For the case of the entire rainfall dataset and for stratiform rainfall, the PDF of A_h is concentrated between 0 and 2.0×10^{-3} $\mathrm{dB\,km^{-1}}$ and that of convective rainfall is strongly concentrated between 1.0×10^{-3} and 8.0×10^{-3} $\mathrm{dB\,km^{-1}}$ (Fig. 4i). Unlike the PDF of A_h for convective rainfall, the PDF for stratiform rainfall shows a strong peak at about 7.0×10^{-4} $\mathrm{dB\,km^{-1}}$.

3.2. Climatological Characteristics of DSD in Busan

The climatological characteristics of DSDs for 10 rainfall categories are analyzed in this study. Sample size and ratio rainfall for each category are summarized in Table 3. Figure 5a illustrates the distribution of all 1-min stratiform rainfall data, and Fig. 5b shows scatter plots of averaged

D_m and $\log_{10}(N_w)$ for all 10 rainfall categories for stratiform rainfall data. Figure 5a displays a remarkable clear boundary in the bottom sector and shows that most of the data lie below the reference line used by Bringi et al. (2003) to classify convective and stratiform rainfall. The average value of D_m and $\log_{10}(N_w)$ for all rainfall categories, except for heavy rainfall, exist between 1.4 and 1.6 mm and between 3.15 to 3.5 ,respectively (Fig. 5b). These values are relatively small compared with the reference line presented by Bringi et al. (2003). However, the average line of $\log_{10}(N_w)$ for each rainfall type extends beyond the reference line when D_m is greater than 1.7 mm (figure not shown), which is similar to the results from Järvenpää, Finland (Fig.14 of Leinonen et al., 2012).

The distribution of 1-min convective rainfall data is displayed in Fig. 6a and the distribution of average values of D_m and N_w for the 10 rainfall categories in the case of convective rainfall in Fig. 6b. The blue and red plus symbols represent maritime and continental rainfall, respectively, as defined by Bringi et al. (2003). The scatter plot of 1-min convective rainfall data shows more in the continental cluster than the maritime cluster; however, the average values for the 10 rainfall categories are all located around the maritime cluster, except for the Typhoon category. By considering the entire average values including Typhoon event (Fig. 6b), we can induce the simple linear equation using D_m and $\log_{10}(N_w)$ as follows:

$$\log_{10}(N_w) = -1.8D_m + 6.9. \qquad (16)$$

The D_m (N_w) value for the Typhoon category was considerably smaller (larger) than that of the other categories as well as that of stratiform type of Typhoon. This result does not agree with that reported by Chang et al. (2009), who noted that the D_m of convective rainfall Typhoon showed a large value compared with that associated with stratiform rainfall.

3.3 Diurnal Variation in Raindrop Size Distributions

3.3.1. Diurnal Variations in DSDs

Figure 7a shows a histogram of normalized frequency of 16 wind directions recorded by the AWS, which is the same instrument as that used to collect the data shown in Fig. 3. To establish the existence of a land and sea wind, the difference in wind direction frequencies between DT and NT were analyzed. Figure 7b shows the difference between DT and NT, difference frequency means normalized frequency of wind direction for DT subtract to that of NT for each direction, in terms of the normalized frequency of 16 wind directions. In other word, positive (negative) values indicate that the frequency of wind is higher in the DT (NT). Also, land (sea) wind defined in present study from 225° (45°) to 45° (225°) according to the geographical condition in Busan. The predominant frequency of wind direction in the DT (NT), between 205° (22.5°) and 22.5° (205.5°), is higher than that in the NT (DT) (Fig. 7b). The observation site where the POSS was installed at western side from the closest coast line, distance is about 611 m, suggesting that the effect of the land and sea wind would have been recorded.

To understand the effects of the land and sea wind on DSD characteristics, we analyzed the PDF and 2-hour averaged DSD parameters for DT and NT. Figure 8 illustrates the distributions of μ, D_m, $\log_{10}(N_w)$, $\log_{10}(LWC)$, $\log_{10}(R)$, and Z. There were large variations of μ with time. The μ values varied from 2.41 to 3.17 and the minimum and maximum μ values occurred at 0800 KST and 1200 KST, respectively (Fig. 8a). A D_m larger than 1.3 mm dominated from 0000 KST to 1200 KST, before decreasing remarkably between 1200 and 1400 KST. The minimum and maximum $\mathrm{D_m}$ appeared at 1400 KST and 0800 KST, respectively (Fig. 8b).

$\mathrm{N_w}$ generally varies inversely to $\mathrm{D_m}$; however, no inverse relationship was identified between $\mathrm{D_m}$ and $\mathrm{N_w}$ in case of the time series (Fig. 8c). The maximum and minimum values of $\mathrm{N_w}$ were found at 0600 KST and 2200 KST.

Variability through time was similar for R, LWC, and $\mathrm{Z_h}$ as $\mathrm{D_m}$. There was an increasing trend from 0000 KST to 0800 KST followed by a remarkably decreasing trend from 0800 KST to 1400 KST (Figs 8d, 11e and 11f). Note that the time of the sharp decline for R between 1200 KST and 1400 KST is simultaneous with a $\mathrm{D_m}$ decrease. Larger (smaller) drops would contribute to higher R in the morning (afternoon). These variations considerably matched with the diurnal sea wind time series (Fig. 8g). Sea wind is the sum value of normalized wind frequency between 45° and 225°. From 0200 (1400) KST to 1200 (2000) KST shows smaller (larger) value of sea wind frequency which is opposite to the relatively larger (smaller) parts of each parameter (D_m, R, LWC and Z_h).

The PDF distribution of μ between -2 and 0 is more concentrated for NT than for DT. Furthermore, when $\mu > 0$, DT and NT frequency distributions are similar (Fig. 9a). A larger $N(D)$ of small or large raindrops would be expected in NT than in DT.

The distribution of DT $D_m < 0.7\ mm$ is wider than that of the NT. However, between 0.7 and 1.5 mm the frequency for NT is higher than that for DT, whereas the distribution in the range > 1.5 mm is similar for both DT and NT (Fig. 9b). We note that the smaller peak of D_m around 0.6 mm for the entire rainfall dataset (Fig. 4b) was observed only in DT.

The distribution of $log_{10}(N_w)$ for DT has higher value of PDF at larger $log_{10}(N_w)$ than that of NT at $log_{10}(N_w)$ > 4 (Fig. 9c).

Bringi et al. (2003) noted that the maritime climatology displayed larger N_w and smaller D_m values than the continental climatology, based on observed DSDs in the low and middle latitude. Also, Göke et al. (2007) emphasized that rainfall type can be defined by the origin location and movement direction. In accordance with these previous results, we consider NT rainfall in the Busan region to be more likely caused by a continental convective system.

In the present study, the shape of the PDF of LWC and R for DT and NT are similar which is the same reason with the results of Fig. 4e-f. LWC and R distributions during the DT (NT) are higher (lower) than in the NT (DT) when $log_{10}(LWC)$) and $log_{10}(R)$ are larger (smaller) than -1.2 and 0 , respectively (Fig. 9d and e). The Z has similar pattern with LWC and R during the DT (NT) was higher (lower) than in the NT (DT) in the range below (above) about 27 dBZ (Fig. 9f).

3.3.2. Diurnal Variations of DSDs with respect to Season

Busan experiences distinct atmospheric conditions that are caused by the different frequencies and magnitudes of land and sea winds in response to variable sunrise and sunset times. To identify seasonal variations of DSDs with respect to the effect of the land and sea wind, we analyzed the DT and NT PDF of D_m and N_w in the Summer and Winter. The start and end times of DT (NT) were sorted using the latest sunrise (sunset) and the earliest sunset (sunrise) time for each season (Table 4) which is same method that of entire period classification.

Figure 10a shows a histogram of wind directions in Summer (light grey) and Winter (dark grey). The frequencies of Summer and Winter wind directions are similar to each other. However, in Fig. 10b, the DT and NT distributions of Winter wind direction display opposing frequencies.

Note that Winter season shows remarkable frequency of land (sea) wind between 0° (157.5°) and 45° (202.5°) at DT (NT) compared with results of those for Summer season. The accumulated value of normalized wind frequencies at the sea and land wind show different feature between Summer and Winter season (Table 5).

To identify the variability of DSDs caused by the land and sea wind in Summer and Winter, a 2-hour interval time series of D_m, N_w and R was analyzed. In the Summer, the time series of D_m displays considerably large values between 0000 KST and 1200 KST, compared with the period between 1400 KST and 2200 KST (Fig. 11a). The mean value of D_m decreases dramatically between 1200 KST and 1400 KST. $log_{10}(N_w)$ generally has a negative relationship with D_m (Fig. 11b). However, the inverse relation between $log_{10}(N_w)$ and D_m is not remarkable. The $log_{10}(R)$ tends to increase gradually from 0000 KST to 0800 KST and decrease from 0800 KST to 1400 KST, which is similar to the pattern that of entire period (Fig. 11c). Kozu et al. (2006) analyzed the diurnal variation in R at Gadanki (South India), Singapore, and Kototabang (West Sumatra) during the Summer monsoon season. All regions displayed maximum R at approximately 1600 LST, except for Gadanki. Also, Qian (2008), who analyzed the diurnal variability of wind direction and R on Java Island during the Summer season using 30 years (from 1971 to 2000) of NCEP/NCAR reanalyzed data. They found that a land wind occurred from 0100 LST to 1000 LST and a sea wind from 1300 LST to 2200 LST (Fig. 7 of Qian (2008)). Normalized wind frequency for each direction is similar pattern to the results of Qian (2008) but pattern of R is different with that of Kozu et al. (2006). From 0200 (1200) KST to 1000 (2000) KST shows relatively smaller (larger) frequencies of sea wind. It is different pattern with R. However, these patterns matched with the time series of D_m and $log_{10}(N_w)$. Larger frequency of sea wind direction shows counter-proportional

(proportional) relationship to the smaller (larger) frequency of D_m ($log_{10}(N_w)$). Variability of the D_m time series for Winter is the inverse of the Summer time series (Fig. 11a). The mean value of D_m steadily increases from 0000 KST to 1600 KST and then decreases from 1600 KST to 2200 KST. The Winter $log_{10}(N_w)$ time series displays a clear inverse pattern compared with the D_m variation with time and increases from 1600 KST to 0400 KST and then steadily decreases from 0400 KST to 1600 KST (Fig. 11b). The peak of $log_{10}(N_w)$ occurs at 0400 KST. However, the time series of $log_{10}(R)$ for Winter season shows similar pattern with that of Summer unlike to another parameters (Fig. 11c). Based on the diurnal variation of R, the variations of $\mathrm{D_m}$ and $\mathrm{N_w}$ would be independent to R.

Alike to the D_m and $log_{10}(N_w)$, normalized wind frequency of wind direction for Winter season shows inverse relationship to that of Summer season (Fig. 11d). The value of frequency generally decreases (increases) from 0400 (1400) KST to 1400 (0400) KST. Also, it shows symmetry pattern with that of Summer season.

The PDF distribution of Summer D_m displays a relatively large DT frequency compared with NT when D_m < 1.65 mm, except for the range between 0.6 and 0.9 mm. However, in the range of D_m > 1.65 mm, the NT PDF displays a larger frequency (Fig. 12a). The PDF of $log_{10}(N_w)$ for DT (NT) has a larger frequency than the NT (DT) when $log_{10}(N_w)$ > (<) 3.3 but smaller frequency when $log_{10}(N_w)$ < (>) 3.3 (Fig. 12c).

The DT and NT PDFs of D_m and $log_{10}(N_w)$ during Winter display an inverse distribution to that of Summer. For the PDF of D_m, there is a considerable frequency for NT (DT) when D_m < (>) 1.6 mm (Fig. 12b). The PDF of $log_{10}(N_w)$ of Summer season for NT (DT) is larger than that of the DT when $log_{10}(N_w)$ < (>) 3.5 (Fig. 12d). In the PDF analysis, relatively large (small) D_m and small (large) $log_{10}(N_w)$ are displayed during the NT (DT) when a land wind (sea wind) occurs.

Bringi et al. (2003) referred that the convective rainfall type is able to classify as the continental and maritime-like precipitation using D_m and N_w. As the previous study result, we analyzed the PDF of DSDs for Summer and Winter with respect to convective rainfall type. These feature would be shown more clearly in convective type. The convective rainfall type of PDFs of DT and NT for Summer show similar shape of distribution to that of all rainfall type (Fig. 3a). For the PDF of D_m, there is a more frequency for DT (NT) than NT (DT) when D_m < (>) 2.0 mm except for between 0.7 mm and 1.2 mm (Fig. 13a). The PDF of convective rainfall type's $log_{10}(N_w)$ for DT (NT) has a larger frequency than the NT (DT) when $log_{10}(N_w)$ > (<) 3.4 except for between 4.3 and 5.5 (Fig. 12c). PDF distributions for Winter season show more clear pattern compared with those of the entire rainfall type. The value of PDF for D_m in DT (NT) have considerably larger than NT (DT) when $\mathrm{D_m}$ > (<) 1.9 mm, especially between 2.15 mm and 2.3 mm (Fig. 13b). Also, those for $\mathrm{log_{10}(N_w)}$ in DT (NT) show dramatic values when $\mathrm{log_{10}(N_w)}$ < (>) 3.6. Furthermore, PDF values significantly concentrated on between 3 < $\mathrm{log_{10}(N_w)}$ < 3.2 (Fig. 13d). In short, considering the DSD parameters with wind directions, the maritime (continental)-like precipitation would depend on the sea (land) wind.

4. Summary and Conclusion

Climatological characteristics of DSDs in Busan were analyzed using the DSD data observed by POSS over a four-year period from February 24th 2001 to December 24th 2004. Observed DSDs were filtered to remove error by performing several quality control measures, and an AWS rain gauge installed nearby was used to verify the rainfall amount recorded by the POSS.

We analyzed DSD characteristics of convective and stratiform rainfall types, as defined by Bringi et al. (2003). The rainfall dataset was thus divided into stratiform and convective rainfall and their contributions to the total rainfall were 62.93% and 6.11%, respectively. Also, to find the climatological characteristics of DSD for rainfall case, the entire rainfall data was classified as 10 rainfall categories including the entire period case.

According to the study by Bringi et al. (2003), the rainfall in Busan shows maritime climatological DSD characteristics. The mean values of D_m and N_w for stratiform rainfall are relatively small compared with the average line of stratiform rainfall produced by Bringi et al. (2003), except for heavy rainfall events and those for convective type converged around the maritime cluster, except for the Typhoon category. The convective rainfall associated with a Typhoon has considerably smaller D_m and larger N_w values compared with the other rainfall categories. This is likely caused by increased raindrop break-up as a result of strong wind effects. Furthermore, the distributions of mean D_m and N_w values for all rainfall categories associated with convective rainfall display a linear relationship including the Typhoon category.

The analysis of diurnal variation in DSD yielded the following results: first, in the negative range of μ, the frequency of μ is higher at NT than during the DT. The PDF of R is higher at NT than during the DT when $\log_{10}(R) > 0.6$. A gentle peak of D_m was identified during the DT at approximately 0.6 mm. Additionally, the frequency of D_m is higher at NT than during the DT when $D_m > 0.7$ mm. For N_w, which tends to be inversely related to D_m, its frequency is higher at NT than during the DT when $\log_{10}(N_w) > 4$. At NT, D_m is higher and R, μ, and N_w values are lower compared with the DT. This feature is matched with the time series of normalized frequency of sea wind which shows inverse relationship to D_m. Smaller D_m is correspond to the larger sea wind frequency. In short, maritime (continental) –like precipitation are observed in the DT (NT) more often than in the NT (DT), based on the results of Bringi et al. (2003) and wind direction. The above-mentioned DSD characteristics are likely due to the land and sea wind caused by differences in specific heat between the land and ocean. These features are also apparent in the seasonal diurnal distribution. The PDF of DT and NT for convective rainfall type during the Summer is similar to the PDF of the entire period; however, those of the Winter displays the significant inverse distribution compared to Summer because of obvious seasonal differences in wind direction.

Author contributions

Cheol-Hwan You designed the study. Sung-Ho Suh modified the original study theme and performed the study. Cheol-Hwan You and Sung-Ho Suh performed research, obtained the results and prepared the manuscript along with contributions from all of the co-authors. Dong-In Lee examined the results and checked the manuscript.

Acknowledgement

This work was funded by the Korea Meteorological Industry Promotion Agency under Grant KMIPA 2015-1050

References

Andsager, K., Beard, K. V., and Laird, N. F.: Laboratory measurements of axis ratios for large raindrops, Journal of the Atmospheric Sciences, 56, 2673-2683, 1999.

Atlas, D., Srivastava, R., and Sekhon, R. S.: Doppler radar characteristics of precipitation at vertical incidence, Reviews of Geophysics, 11, 1-35, 1973.

Atlas, D., Ulbrich, C. W., Marks, F. D., Amitai, E., and Williams, C. R.: Systematic variation of drop size and radar-rainfall relations, Journal of Geophysical Research: Atmospheres (1984–2012), 104, 6155-6169, 1999.

Beard, K. V., and Chuang, C.: A new model for the equilibrium shape of raindrops, Journal of the Atmospheric sciences, 44, 1509-1524, 1987.

Brandes, E. A., Zhang, G., and Vivekanandan, J.: Experiments in rainfall estimation with a polarimetric radar in a subtropical environment, Journal of Applied Meteorology, 41, 674-685, 2002.

Bringi, V., Chandrasekar, V., Hubbert, J., Gorgucci, E., Randeu, W., and Schoenhuber, M.: Raindrop size distribution in different climatic regimes from disdrometer and dual-polarized radar analysis, Journal of the atmospheric sciences, 60, 354-365, 2003.

Chang, W.-Y., Wang, T.-C. C., and Lin, P.-L.: Characteristics of the raindrop size distribution and drop shape relation in Typhoon systems in the western Pacific from the 2D video disdrometer and NCU C-band polarimetric radar, Journal of Atmospheric and Oceanic Technology, 26, 1973-1993, 2009.

Dou, X., Testud, J., Amayenc, P., and Black, R.: The parameterization of rain for a weather radar, Comptes Rendus de l'Académie des Sciences-Series IIA-Earth and Planetary Science, 328, 577-582, 1999.

Feingold, G., and Levin, Z.: The lognormal fit to raindrop spectra from frontal convective clouds in Israel, Journal of Climate and Applied Meteorology, 25, 1346-1363, 1986.

Göke, S., Ochs III, H. T., and Rauber, R. M.: Radar analysis of precipitation initiation in maritime versus continental clouds near the Florida coast: Inferences concerning the role of CCN and giant nuclei, Journal of the Atmospheric Sciences, 64, 3695-3707, 2007.

Gamache, J. F., and Houze Jr, R. A.: Mesoscale air motions associated with a tropical squall line, Monthly Weather Review, 110, 118-135, 1982.

Gunn, R., and Kinzer, G. D.: The terminal velocity of fall for water droplets in stagnant air, Journal of Meteorology, 6, 243-248, 1949.

Hu, Z., and Srivastava, R.: Evolution of raindrop size distribution by coalescence, breakup, and evaporation: Theory and observations, Journal of the atmospheric sciences, 52, 1761-1783, 1995.

Johnson, R. H., and Hamilton, P. J.: The relationship of surface pressure features to the precipitation and airflow structure of an intense midlatitude squall line, Monthly Weather Review, 116, 1444-1473, 1988.

Kozu, T., Reddy, K. K., Mori, S., Thurai, M., Ong, J. T., Rao, D. N., and Shimomai, T.: Seasonal and diurnal variations of raindrop size distribution in Asian monsoon region, JOURNAL-METEOROLOGICAL SOCIETY OF JAPAN SERIES 2, 84, 195, 2006.

Leinonen, J., Moisseev, D., Leskinen, M., and Petersen, W. A.: A climatology of disdrometer measurements of rainfall in Finland over five years with implications for global radar observations, Journal of Applied Meteorology and Climatology, 51, 392-404, 2012.

Levin, Z.: Charge separation by splashing of naturally falling raindrops, Journal of the Atmospheric Sciences, 28, 543-548, 1971.

Mapes, B. E., and Houze Jr, R. A.: Cloud clusters and superclusters over the oceanic warm pool, Monthly Weather Review, 121, 1398-1416, 1993.

Markowitz, A. H.: Raindrop size distribution expressions, Journal of Applied Meteorology, 15, 1029-1031, 1976.

Marshall, J. S., and Palmer, W. M. K.: The distribution of raindrops with size, Journal of meteorology, 5, 165-166, 1948.

Mueller, E. A.: Radar cross sections from drop size spectra, University of Illinois at Urbana-Champaign, 1966.

Pruppacher, H., and Beard, K.: A wind tunnel investigation of the internal circulation and shape of water drops falling at terminal velocity in air, Quarterly Journal of the Royal Meteorological Society, 96, 247-256, 1970.

Qian, J.-H.: Why precipitation is mostly concentrated over islands in the Maritime Continent, Journal of the Atmospheric Sciences, 65, 1428-1441, 2008.

Ray, P. S.: Broadband complex refractive indices of ice and water, Applied Optics, 11, 1836-1844, 1972.

Sauvageot, H., and Lacaux, J.-P.: The shape of averaged drop size distributions, Journal of the Atmospheric Sciences, 52, 1070-1083, 1995.

Seliga, T., and Bringi, V.: Potential use of radar differential reflectivity measurements at orthogonal polarizations for measuring precipitation, Journal of Applied Meteorology, 15, 69-76, 1976.

Sheppard, B. E.: Measurement of raindrop size distributions using a small Doppler radar. J. Atmos. Oceanic Technol., 7, 255–268, 1990.

Sheppard, B. E. and P. I. Joe: Comparison of raindrop size distribution measurements by a Joss–Waldvogel disdrometer, a PMS 2DG spectrometer and a POSS Doppler radar. J. Atmos. Oceanic Technol., 11, 874–887, 1994.

Sheppard, B., and Joe, P.: Performance of the precipitation occurrence sensor system as a precipitation gauge, Journal of atmospheric and Oceanic technology, 25, 196-212, 2008.

Steiner, M., Houze Jr, R. A., and Yuter, S. E.: Climatological characterization of three-dimensional storm structure from operational radar and rain gauge data, Journal of Applied Meteorology, 34, 1978-2007, 1995.

Testud, J., Oury, S., Black, R. A., Amayenc, P., and Dou, X.: The concept of "normalized" distribution to describe raindrop spectra: A tool for cloud physics and cloud remote sensing, Journal of Applied Meteorology, 40, 1118-1140, 2001.

Tokay, A., and Short, D. A.: Evidence from tropical raindrop spectra of the origin of rain from stratiform versus convective clouds, Journal of applied meteorology, 35, 355-371, 1996.

Ulbrich, C. W.: Natural variations in the analytical form of the raindrop size distribution, Journal of Climate and Applied Meteorology, 22, 1764-1775, 1983.

Ulbrich, C. W., and Atlas, D.: Rainfall microphysics and radar properties: Analysis methods for drop size spectra, Journal of Applied Meteorology, 37, 912-923, 1998.

Waldvogel, A.: The N 0 jump of raindrop spectra, Journal of the Atmospheric Sciences, 31, 1067-1078, 1974.

Waterman, P.: Symmetry, unitarity, and geometry in electromagnetic scattering, Physical review D, 3, 825, 1971.

Willis, P. T.: Functional fits to some observed drop size distributions and parameterization of rain, Journal of the Atmospheric Sciences, 41, 1648-1661, 1984.

You, C.-H., Lee, D.-I., and Kang, M.-Y.: Rainfall estimation using specific differential phase for the first operational polarimetric radar in Korea, Advances in Meteorology, 2014, 2014.

Zhang, G., Vivekanandan, J., and Brandes, E.: A method for estimating rain rate and drop size distribution from polarimetric radar measurements, Geoscience and Remote Sensing, IEEE

Transactions on, 39, 830-841, 2001.

Tables 1. Specification of POSS disdrometer.

Specifications	Detail
Manufacturer	ANDREW CANADA INC
Module	PROCESSOR
Model number	POSS-F01
Nominal power	100 mW
Bandwidth	Single frequency
Emission	43 mW
Pointing direction	20 ° (to the vertical side)
Antenna	Rectangular pyramidal horns
Range of sample area	< 2 m
Wavelength	10.525 GHz ± 15 GHz
Physical dimension	277×200×200 cm^3
Net weights	Approximately 110 kg

Table 2. Designated date with respect to the source of rainfall.

Rainfall Category	Period			
	2001	**2002**	**2003**	**2004**
Typhoon	-	7.5-7.6, 8.31	5.29, 6.19, 8.7, 9.11-12	6.20, 8.19, 9.6
Chanma	6.18-6.19, 6.23-6.26, 6.29-6.30, 7.1, 7.5-7.6 7.11-7.14	6.23-6.25, 6.30, 7.1-7.2	6.12-6.14, 6.23, 6.27 6.30, 7.1, 7.3-7.15	7.11-7.13, 7.14
Heavy rainfall	02.04.15. 20:13 to 02.04.16 06:29			
Seasonal	**Spring**	**Summer**	**Autumn**	**Winter**
	Mar. to May	Jun. to Aug.	Sep. to Nov.	Dec. to Feb.
Diurnal	**DT (KST)**		**NT (KST)**	
	0733 - 1712		1942 - 0509	

Table 3. Rainfall rate for each rainfall category and the number of sample size for 1-min data.

Rainfall Category	Total precipitation	Stratiform precipitation (%)	Convective precipitation (%)
Typhoon	5095	3118 (61.19)	652 (12.79)
Changma	18526	11099 (59.91)	1611 (8.69)
Heavy rainfall	359	153 (42.61)	150 (41.78)
Spring	30703	20370 (66.34)	1478 (4.81)
Summer	37187	22566 (60.68)	3409 (9.16)
Autumn	19809	12033 (60.74)	850 (4.29)
Winter	11689	7582 (64.86)	339 (2.90)
Daytime	41328	26373 (63.81)	2539 (6.14)
Nighttime	37455	23063 (84.00)	2242 (5.89)
Entire	99388	62551 (62.93)	6076 (6.11)

Table 4. DT and NT (KST) in Summer and Winter season.

Rainfall Category	Period	Beginning time (KST)	Finishing time (KST)
Summer	**DT**	0533	1927
	NT	1942	0509
Winter	**DT**	0733	1712
	NT	1819	0654

Table 5. Sum of the normalized wind direction frequencies between Summer and Winter.

Sum of the normalized wind direction frequencies				
Season	**Summer**		**Winter**	
Type	**Sea wind**	**Land wind**	**Sea wind**	**Land wind**
Frequency	0.4139	0.5861	0.3137	0.6863
Difference of the normalized wind direction frequency between DT and NT (DT-NT)				
Season	**Summer**		**Winter**	
Type	**Sea wind**	**Land wind**	**Sea wind**	**Land wind**
Frequency	0.0731	-0.0731	-0.0697	0.0697

Figures

Figure 1.

Photograph of the POSS instrument used in this research.

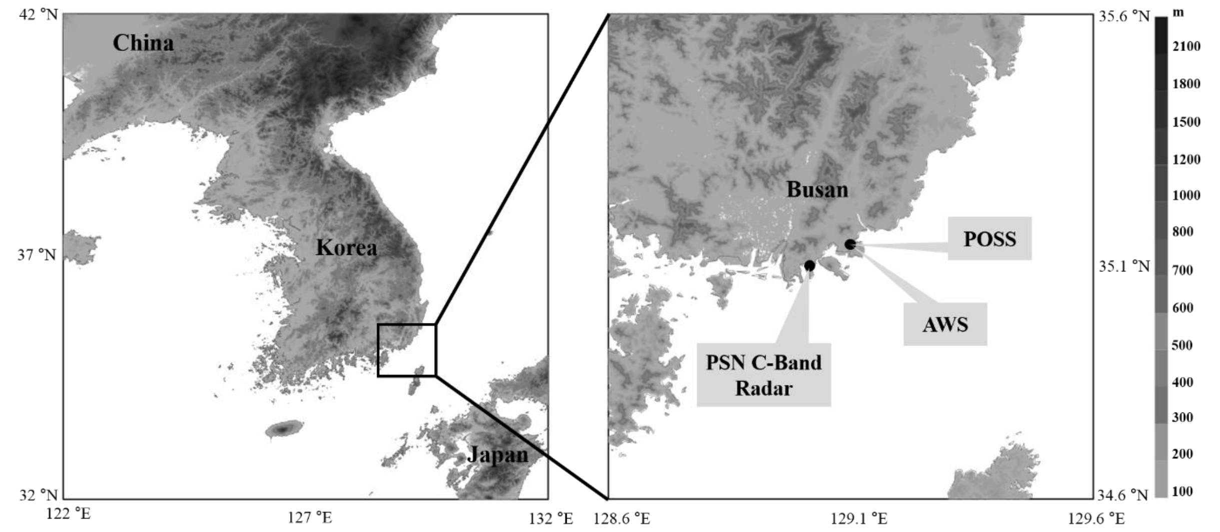

Figure 2.

Locations of the POSS and the AWS rain gauge installed in Busan, Korea.

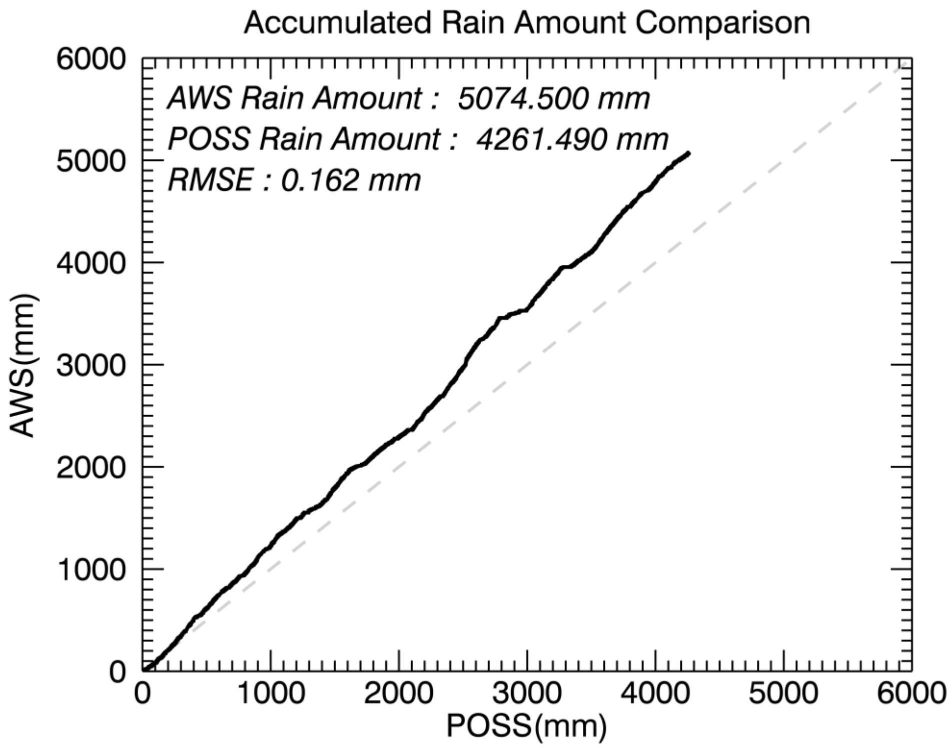

Figure 3.

Comparison of the recorded rainfall amounts between the POSS and AWS instrument.

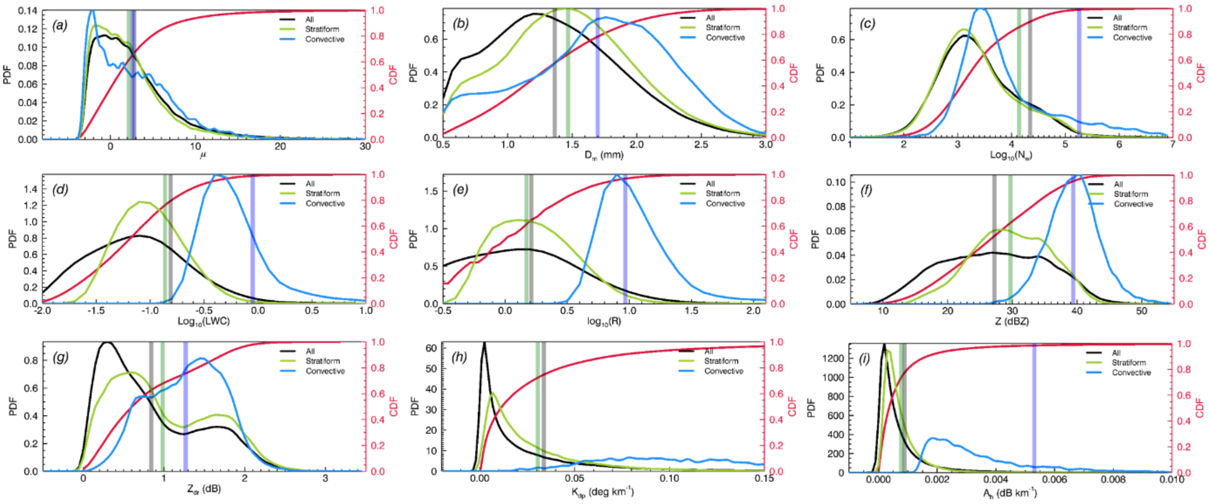

Figure 4.

PDF and CDF curves for (a) μ, (b) $\mathrm{D_m}$, (c) $\log_{10}(\mathrm{N_w})$, (d) $\log_{10}(\mathrm{R})$, (e) $\log_{10}(\mathrm{LWC})$, (f) Z, (g) $\mathrm{Z_{dr}}$, (h) $\mathrm{K_{dp}}$, and (i) $\mathrm{A_h}$ for the entire rainfall dataset (solid black line), stratiform rainfall (solid green line), and convective rainfall (solid blue line. The solid red line represents the CDF for entire rainfall dataset. The solid vertical line represents the mean value of each type.

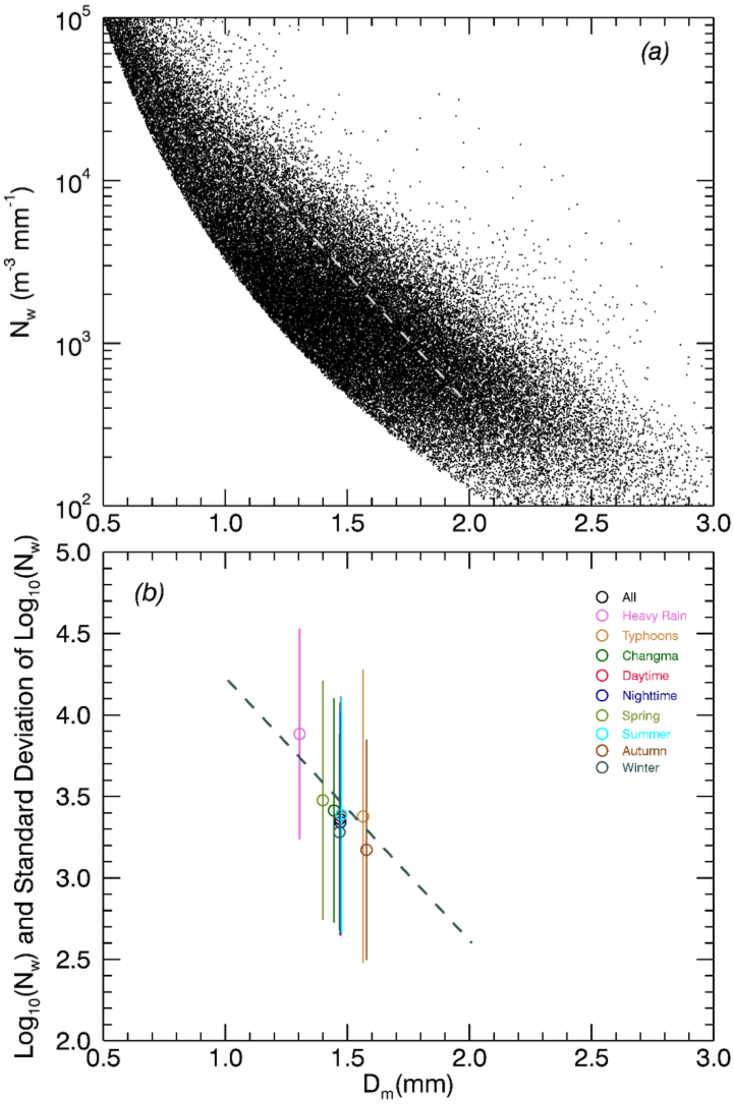

Figure 5.

(a) Scatter plot of 1-min D_m and N_w for the 10 rainfall categories with respect to stratiform rainfall data. The broken grey line represents the average line as defined by Bringi et al. (2003). (b) Scatter plot of mean D_m and $\log_{10}(N_w)$ values of the 10 rainfall categories with respect to stratiform rainfall. The vertical line represents $\pm 1\sigma$ of $\log_{10}(N_w)$ for each category.

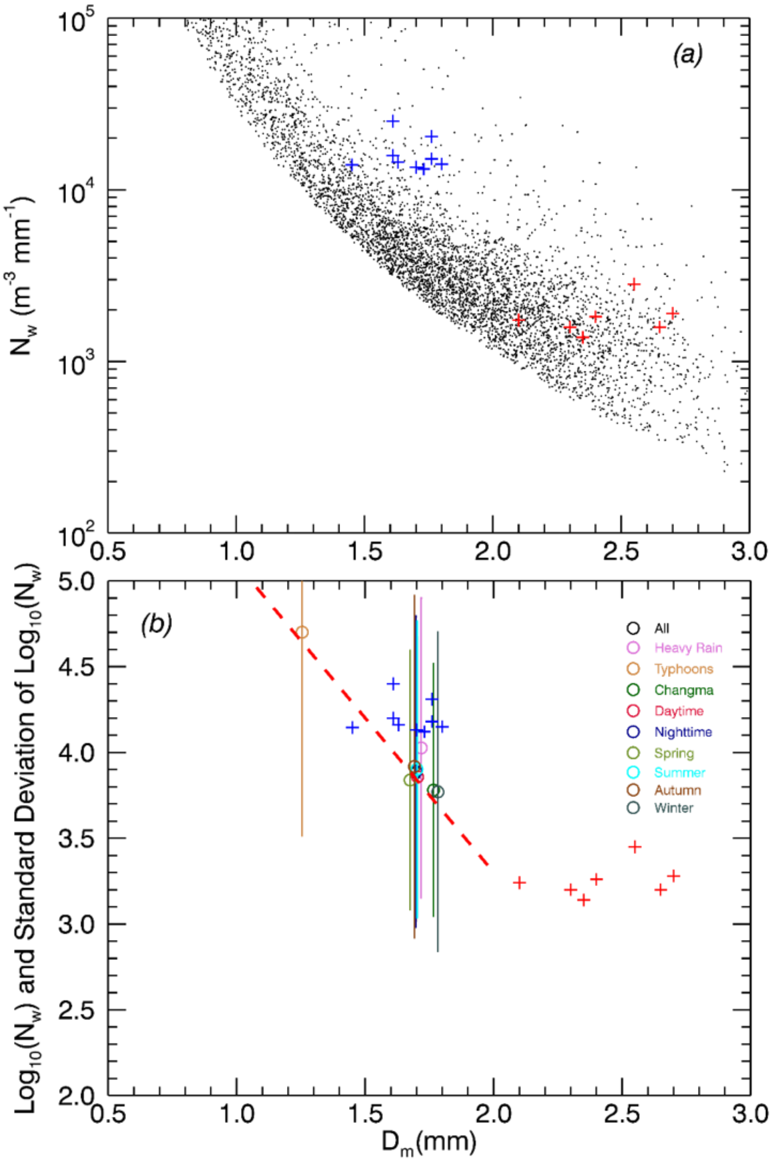

Figure 6.

(a) As in Figure 5(a), but for convective rainfall. The blue and red plus symbols represent maritime and continental rainfall, respectively, as defined by Bringi et al. (2003). (b) As in Figure 5(b), but for convective rainfall. The broken red line represents the mathematical expression described in Eq. (16).

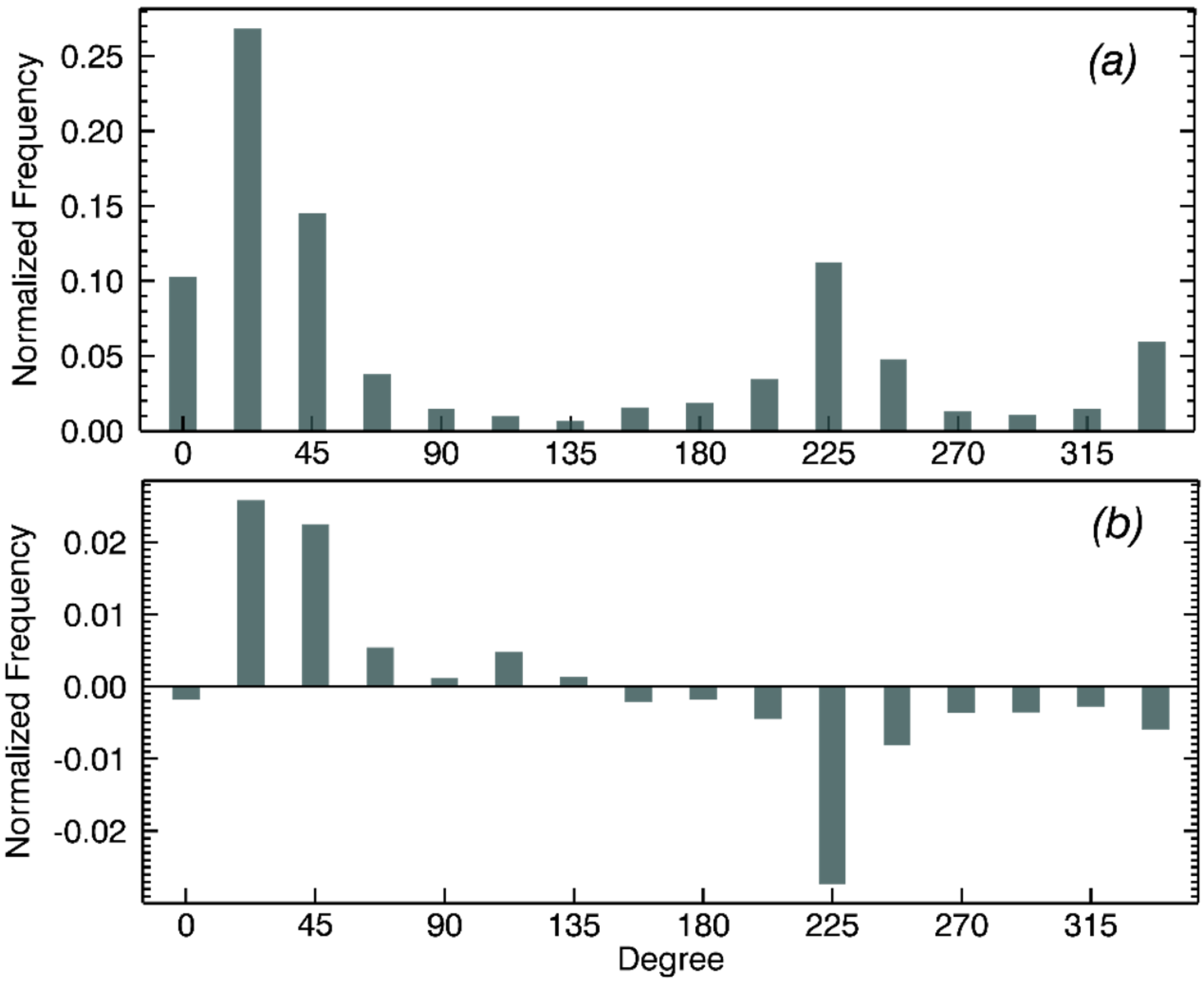

Figure 7

(a) Histogram of normalized frequency of 16 wind directions for the entire study period. (b) Difference values of wind direction frequencies between DT and NT (DT - NT).

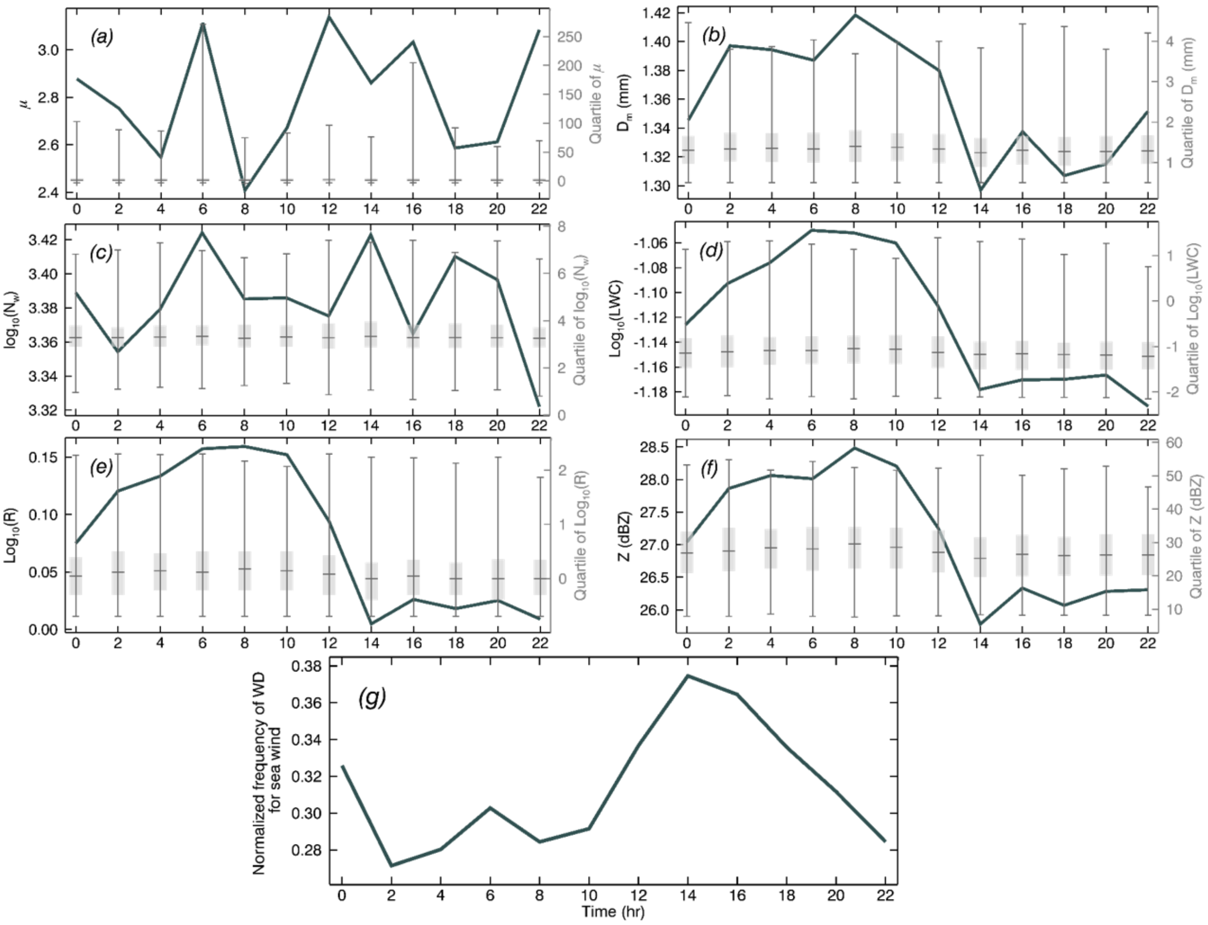

Figure 8.

Two hour interval time series of (a) μ, (b) D_m, (c) $\log_{10}(N_w)$, (d) $\log_{10}(R)$, (e) $\log_{10}(LWC)$, (f) Z_h and (g) normalized frequency of wind direction for sea wind (45° to 225°) with quartiles for the total period. Solid lines are quartiles for each time.

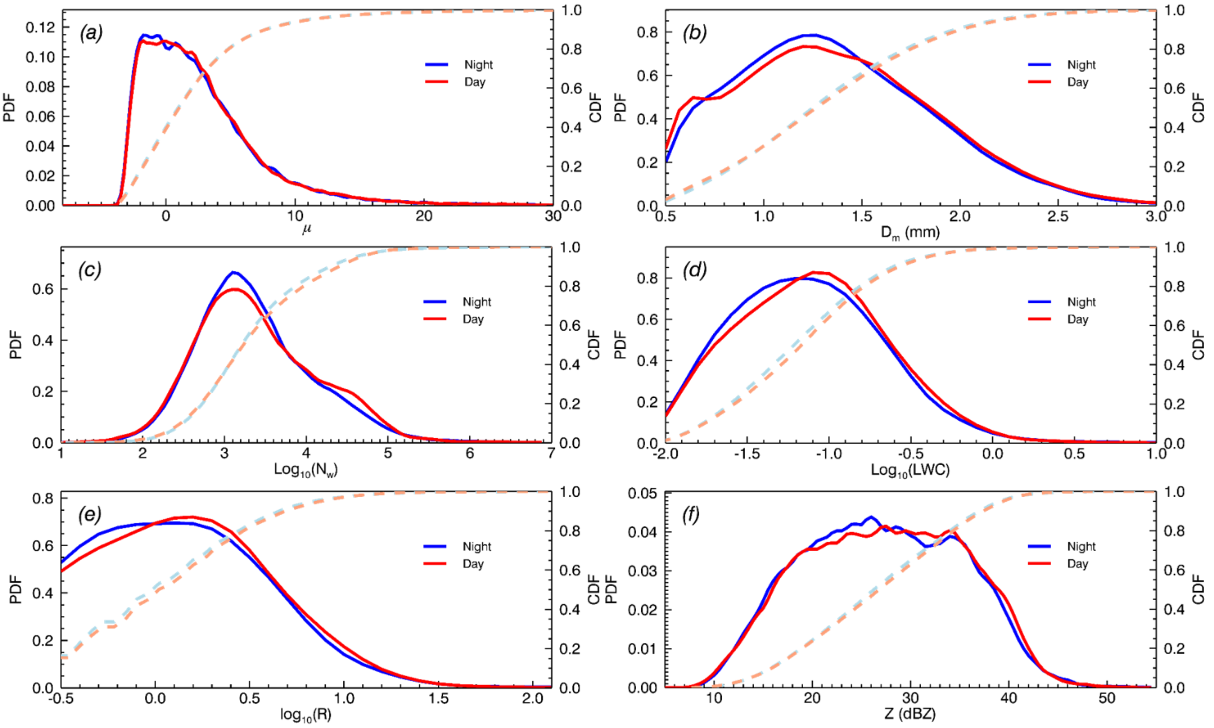

Figure 9.

PDF and CDF curves for (a) μ, (b) D_m, (c) $\log_{10}(N_w)$, (d) $\log_{10}(R)$, (e) $\log_{10}(LWC)$, and (f) Z for DT and NT. The solid red and blue lines represent the PDF for DT and NT, respectively. The broken light red and blue lines represent the CDF for DT and NT, respectively.

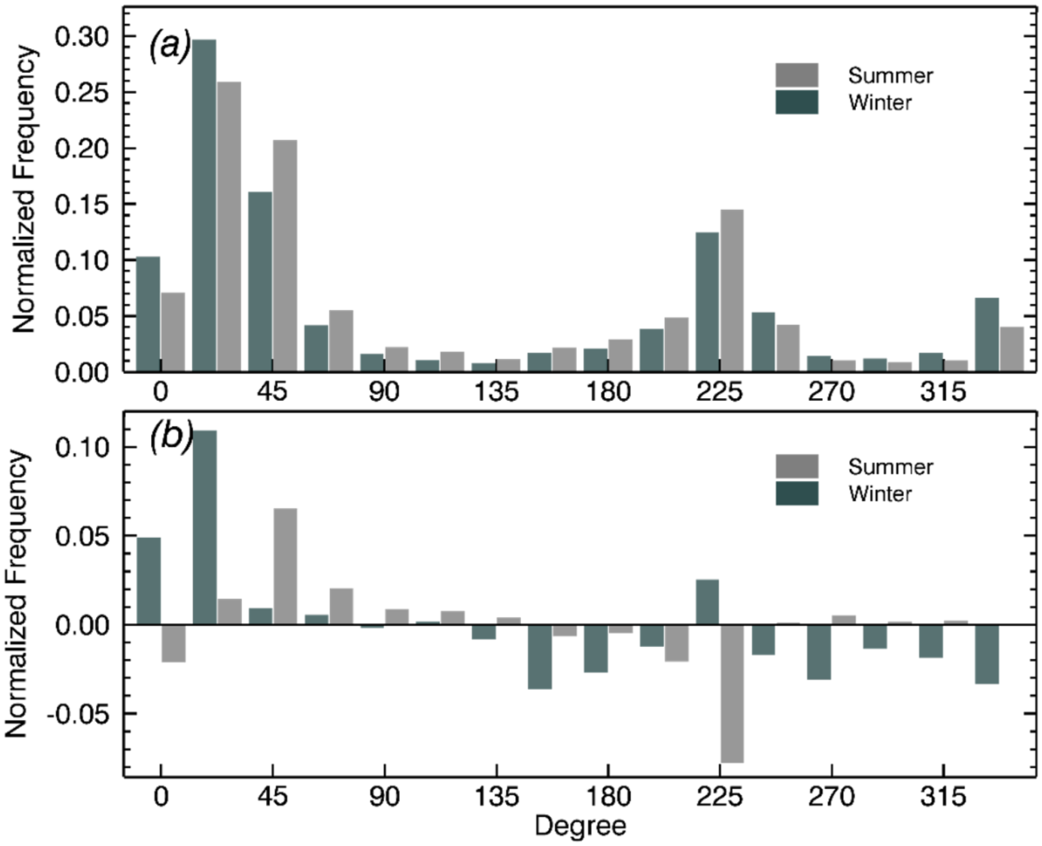

Figure 10.

Histogram of normalized frequency for 16 wind directions in (a) the entire period and (b) difference of normalized frequency of wind direction between DT and NT (DT – NT) for Summer (light grey) and Winter (dark grey) season.

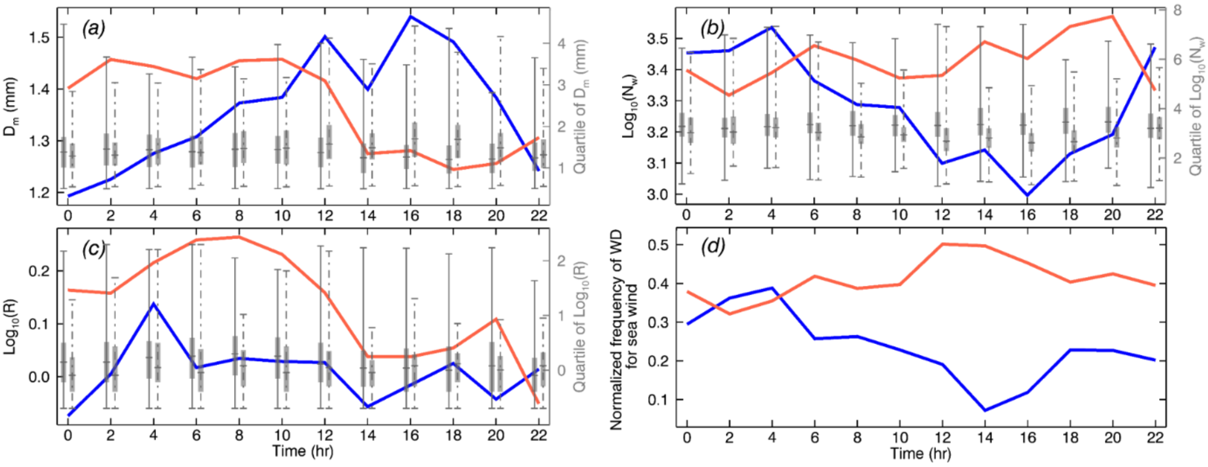

Figure 11.

Two hour interval time series and quartiles of (a) D_m, (b) $\log_{10}(N_w)$ (c) $\log_{10}(R)$ and (d) normalized frequency of wind direction for sea wind (45° to 225°) for the Summer (red) and Winter (blue) season. Solid (broken) lines are quartiles of Summer (Winter) for each time, respectively.

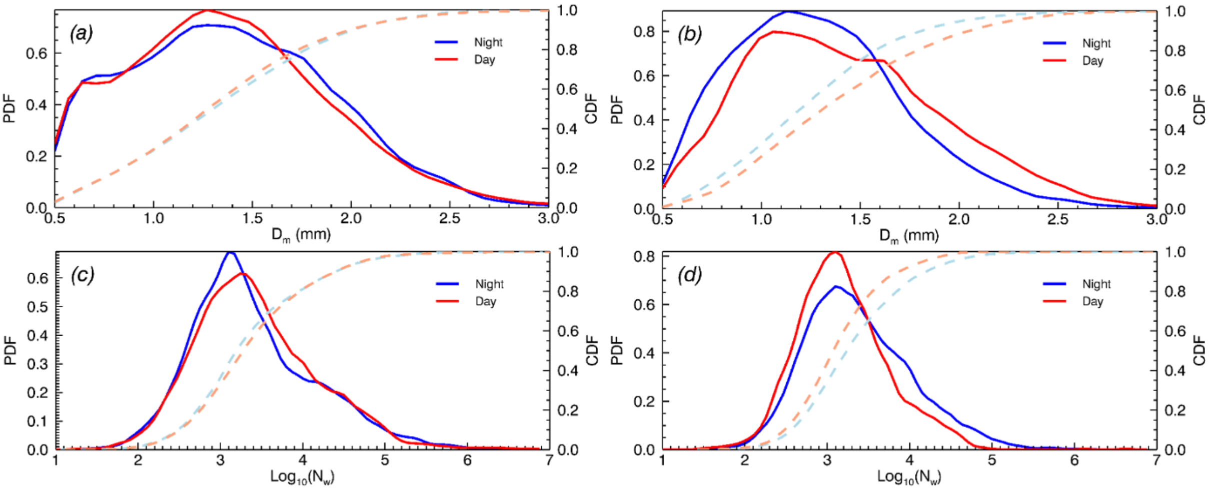

Figure 12.

PDF and CDF of (a) D_m ((b) D_m) and (c) N_w ((d) N_w) in the Summer (Winter) season. Red and blue solid lines represent the PDF of DT and NT, respectively. The light red and blue broken line represent the CDF for each season

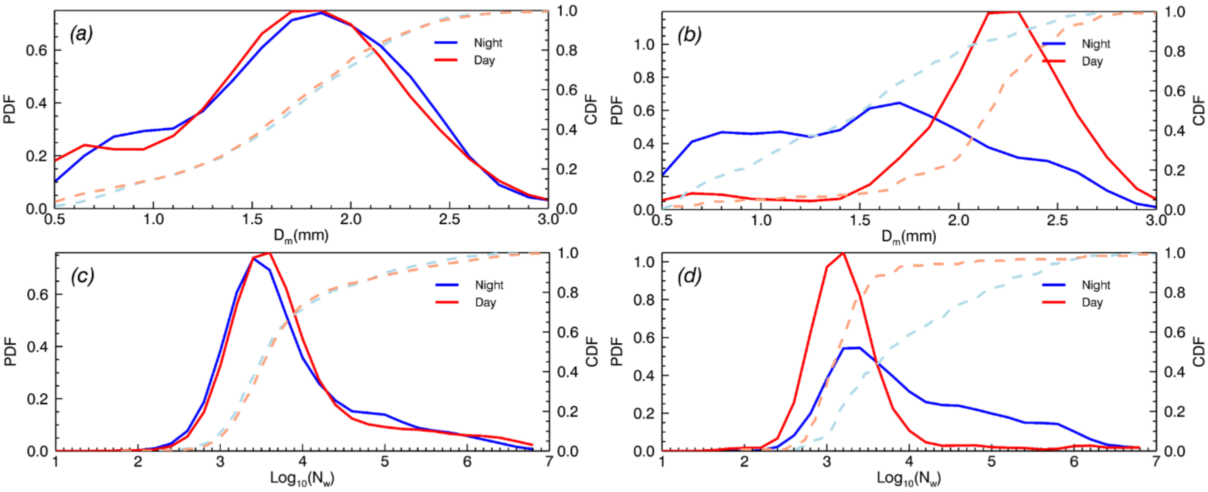

Figure 13.

As in Figure 12, but for convective rainfall type.